

Thermal Feedback in the high-mass star and cluster forming region W51: Massive Protostars like their food well-done

Adam Ginsburg^{1,2}, Ciriaco Goddi^{3,4}, Roberto Galván-Madrid⁵, James E. Dale*, John Bally⁷, Rowan Smith*, Jeremy Darling⁷, J. M. Diederik Kruijssen*, Erik Rosolowsky *, Robert Loughnane⁵, Leonardo Testi^{1,*,*}, Nate Bastian *, Jaime E. Pineda *, Elisabeth Mills *

¹ European Southern Observatory, Karl-Schwarzschild-Straße 2, D-85748 Garching bei München, Germany
e-mail: Adam.Ginsburg@eso.org

² National Radio Astronomy Observatory, Socorro, NM 87801 USA

* Max-Planck-Institut für extraterrestrische Physik, Giessenbachstrasse 1, 85748 Garching, Germany

* INAF-Osservatorio Astrofisico di Arcetri, Largo E. Fermi 5, I-50125, Florence, Italy

* Excellence Cluster Universe, Boltzman str. 2, D-85748 Garching bei München, Germany

³ Department of Astrophysics/IMAPP, Radboud University Nijmegen, PO Box 9010, 6500 GL Nijmegen, the Netherlands

⁴ ALLEGRO/Leiden Observatory, Leiden University, PO Box 9513, 2300 RA Leiden, the Netherlands

⁵ Instituto de Radioastronomía y Astrofísica, UNAM, A.P. 3-72, Xangari, Morelia, 58089, Mexico

* Centre for Astrophysics Research, University of Hertfordshire, College Lane, Hatfield, AL10 9AB, UK

⁷ CASA, University of Colorado, 389-UCB, Boulder, CO 80309

* Jodrell Bank Centre for Astrophysics, School of Physics and Astronomy, University of Manchester, Oxford Road, Manchester M13 9PL, UK

* Astronomisches Rechen-Institut, Zentrum für Astronomie der Universität Heidelberg, Mönchhofstraße 12-14, 69120 Heidelberg, Germany

* Dept. of Physics, University of Alberta, Edmonton, Alberta, Canada

* Astrophysics Research Institute, Liverpool John Moores University, 146 Brownlow Hill, Liverpool L3 5RF, UK

* UCSD TODO finish this

2016/11/16

ABSTRACT

We present ALMA observations of a $\sim 3 \times 1.5$ pc area in the W51 high-mass star-forming complex. We identify dust continuum sources and measure the gas and dust temperature through both rotational diagram modeling and brightness-temperature-based limits. The observed region contains three high-mass YSOs that appear to be at the earliest stages of their formation, with no signs of ionizing radiation from their central sources. The new data reveal high gas and dust temperatures ($T > 100$ K) extending out to about 5000 AU from each of these sources, indicating that the forming MYSOs are able to heat a large volume of gas in which fragmentation is suppressed. No distinct fragments are observed within this heated zone, though 75 sources representing either prestellar cores or some stage of protostars are detected in the observed field. During the process of forming, high-mass stars heat a large volume (and correspondingly large mass) of gas, preventing it from fragmenting, and therefore keep a large reservoir available to feed from. By contrast, more mature massive stars that illuminate compact H II regions have little effect on their surrounding dense gas, hinting that these sources have completed most or all of their accretion. These warm cores are presently stable against Jeans fragmentation, but at their current density and lower temperature, they would not have been, so they must have been assembled from a larger volume of gas.

1. Introduction

High-mass stars are the drivers of galaxy evolution, cycling enriched materials into the interstellar medium (ISM) and illuminating it. During their formation process, however, these stars are nearly undetectable because of their rarity and their opaque surroundings. We therefore know relatively little about how massive stars acquire their mass and what their immediate surroundings look like at this early time.

Assuming the stellar initial mass function (IMF) is a universal (or nearly universal) distribution (Bastian et al. 2010), massive stars O-stars (with $M > 50M_{\odot}$) almost always form in a clustered fashion (in proto-clusters or proto-associations ??Parker & Goodwin 2007). Their presence, and the strong feedback they produce, may directly influ-

ence how the IMF around them is formed. If feedback from these stars is relevant while most of the mass surrounding them is still in gas (not yet in stars), the mass function in such clusters cannot be determined by ISM properties alone.

Models of high-mass star formation universally have difficulty collapsing enough material to a stellar radius to form very massive stars. Generally, these models produce a high-mass star with enough luminosity to halt further *spherical* accretion at a very early stage, with $M_* \sim 10 - 20M_{\odot}$. Radiation pressure provides a fundamental limit on how much mass can be accreted, but geometric effects can circumvent this limit and allow further accretion (Yorke & Sonnhalter 2002; Krumholz et al. 2005, 2009; Krumholz & Matzner 2009; Kuiper & Yorke 2012, 2013; Rosen et al. 2016). Additionally, fragmentation-induced starvation can limit the

Table 5. Spectral Lines in SPW 3

Line Name	Frequency GHz
CH ₃ OH 4 _{2,3} – 5 _{1,4}	234.68345
CH ₃ OH 5 _{-4,2} – 6 _{-4,3}	234.69847
CH ₃ OH 18 _{3,15} – 17 _{4,14}	233.79575
¹³ CH ₃ OH 5 _{1,5} – 4 _{1,4}	234.01158
PN 5 – 4	234.93569
NH ₂ CHO 11 _{5,6} – 10 _{5,5}	233.59451
Acetone 12 _{11,2} – 11 _{10,1} AE	234.86136
SO ₂ 16 _{6,10} – 17 _{5,13}	234.42159
CH ₃ NCO 27 _{2,26} – 26 _{2,25}	234.08812
CH ₃ SH 15 ₂ – 15 ₁	234.19145

are not centrally peaked and are therefore likely to be spatially resolved starless cores.

Further information about and general discussion of the continuum sources is in Appendix C. For the rest of this section, we focus on only the few brightest sources.

3.1.1. W51e2e mass and temperature estimates from continuum

In a $0.21'' \times 0.19''$ beam (1100×1000 au), the peak flux density toward W51 e2e is 0.38 Jy, which corresponds to a brightness temperature $T_B = 225$ K. This is a lower limit to the surface brightness of the millimeter core, since an optical depth $\tau < 1$ or a filling factor of the emission $ff < 1$ would both imply higher intrinsic temperatures. The implied luminosity, assuming blackbody emission from a spherical beam-filling source, is $L = 4\pi r^2 \sigma_{sb} T^4 = 2.3 \times 10^4 L_\odot$. Since any systematic uncertainties imply a higher temperature, this estimate is a lower limit on the source luminosity. Such a luminosity corresponds to a B0.5V, $15 M_\odot$ star with effective temperature 4×10^4 K (Pecaut & Mamajek 2013, see Section 4.3 for further discussion of stellar types).

If we assume that the dust is optically thick throughout our beam, and assume an opacity constant $\kappa(226\text{GHz}) = 120 \text{ g cm}^{-2}$, the minimum mass per beam to achieve $\tau \geq 1$ is $M = 18 M_\odot \text{ beam}^{-1}$. This mass is not a strict limit in either direction: if the dust is indeed optically thick, there may be substantial hidden or undetected gas, while if the filling factor is lower than 1, the dust may be much hotter and therefore optically thin and lower mass. However, simulations and models both predict that the dust will become highly optically thick at radii $r \lesssim 1000$ au (Forgan et al. 2016; Klassen et al. 2016), so it is likely that this measurement provides a lower limit on the total gas mass surrounding the protostar. Therefore, unless the stars are extremely efficient at removing material or the gas fragments significantly on < 1000 AU scales, the stellar mass is likely to at least double before accretion halts.

For an independent measurement of the temperature that is not limited to the optically thick regions, we use the CH₃OH lines in band, calculating an LTE temperature that is $200 < T < 600$ K out to $r < 2''$ ($r < 10^4$ au; Section 3.4). As noted in Section 3.4, these temperatures may be overestimates when the low-J lines of CH₃OH are optically thick, but for now they are the best measurements we have available. If the dust temperature matches the methanol temperature, it would be optically thin ($\tau \lesssim 1/3$) and the

central source dust mass would be only $\sim 6 M_\odot$. However, this latter estimate discounts any substructure at scales < 1000 AU, which we know exists from the 2015.1.01596.S data.

An upper limit on the radio continuum emission from W51e2e is $S_{14.5\text{GHz}} < 0.6 \text{ mJy/beam}$ in a FWHM=0.34'' beam, or $T_{B,max} < 30 \text{ K}$ (Ginsburg et al. 2016b). Assuming emission from an optically thick H II region with $T_e = 8500$ K (Ginsburg et al. 2015), the upper limit on the emitting radius is $R_{\text{HII}} < 110 \text{ AU}$. Similar limits are obtained from other frequencies in those data. The free-free contribution to the millimeter flux is therefore negligible, and the central source is unlikely to be ionizing. Limits on the stellar properties are further discussed in Section 4.3.

3.1.2. W51 e8 and north mass and temperature from continuum

We repeat the above analysis for e8 and north. They have peak flux densities of 0.35 and 0.44 Jy/beam respectively, corresponding to peak brightness temperatures of 205 and 256 K. The lower limit luminosities of W51 e8 and north in a single beam, assuming the brightest detected beam is optically thick, are 1.6×10^4 and $3.9 \times 10^4 L_\odot$, respectively.

W51 North has an upper limit similar to that of W51e2e, but somewhat less restrictive because the noise in that region is substantially higher. W51 e8, by contrast with the others, has a clear detection at cm wavelengths. The source e8n, which is offset from the peak mm emission by 0.13'' (700 AU), has $S_{25\text{GHz}} = 4.7 \text{ mJy/beam}$, corresponding to $T_B = 135 \text{ K}$, which implies an optically thick H II region size $R = 180 \text{ AU}$. This could be part of an ionized jet or an ionizing binary companion, but its offset from the central mm source suggests that it is not a simple spherically symmetric HCH II region.

3.2. The mass and light budget on different spatial scales

An evolutionary indicator used for star-forming regions is the amount of mass at a given density; a more evolved (or more efficiently star-forming) region will have more mass at high densities. We cannot measure the dense gas fraction directly, but the amount of flux density recovered by an interferometer provides an approximation.

For the “total” flux density in the region, we use the Bolocam Galactic Plane Survey observations (Aguirre et al. 2011; Ginsburg et al. 2013), which are the closest in frequency single-dish millimeter data available. We assume a

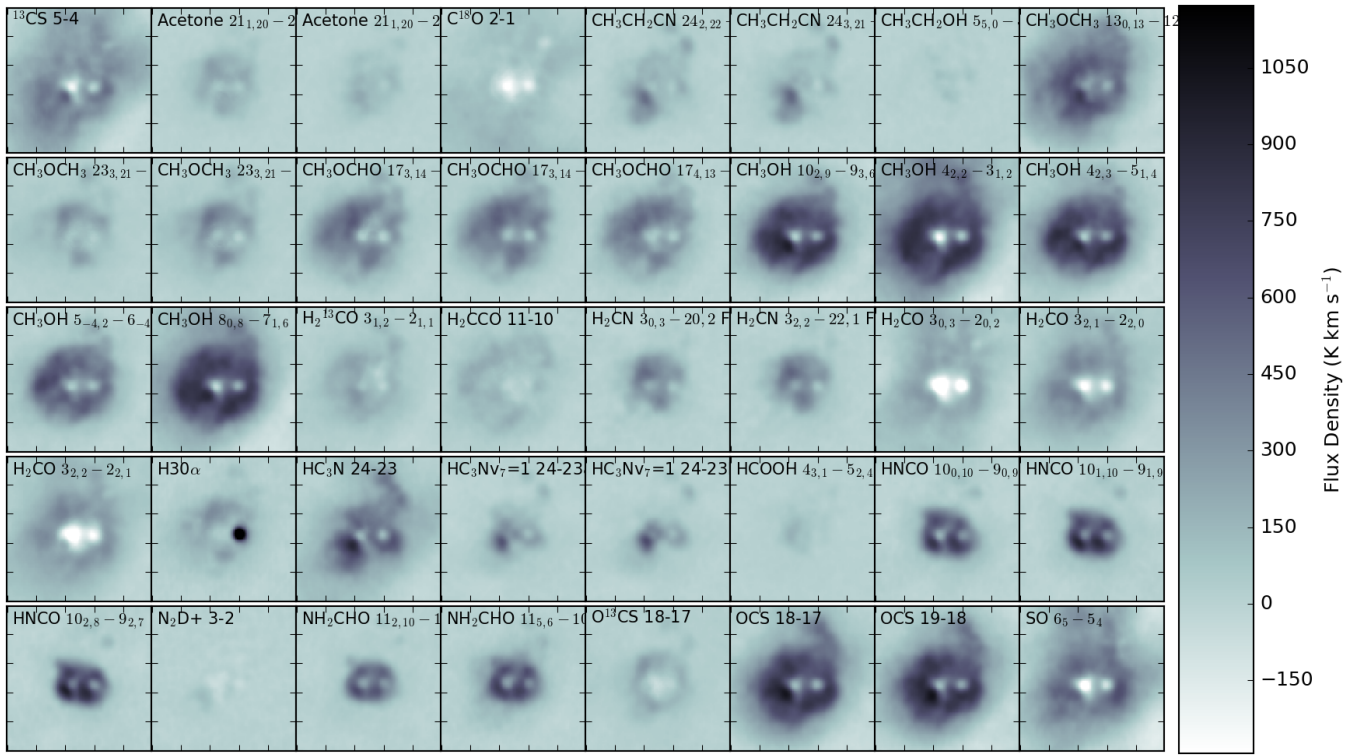


Fig. 2. Moment 0 maps of the e2 region in 40 different lines over the range 51 to 60 km s⁻¹ with continuum subtraction using the 30th percentile emission over the ranges 25-40 and 75-90 km s⁻¹. All images are on the same scale, and the negative features show absorption against the continuum. There is a strong ‘halo’ of emission seen in the CH₃Ox lines and OCS. Extended emission is also clearly seen in SO, ¹³CS, and H₂CO, though these lines more smoothly blend into their surroundings. HNCO and NH₂CHO have smaller but substantial regions of enhancement with a sharp contrast to their surroundings. HC₃N traces the e2 outflow. The bright H30 α emission marks the position of e2w, the hypercompact HII region that dominates the centimeter emission in e2.

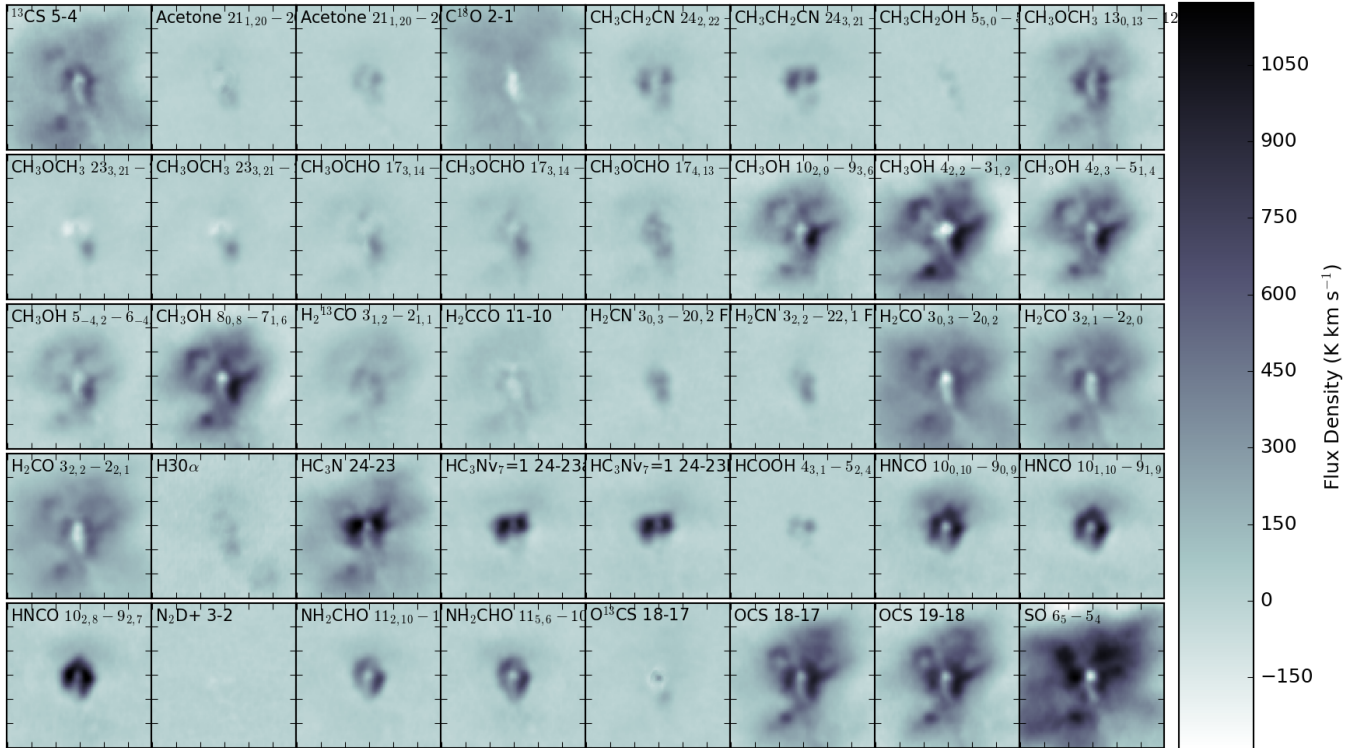


Fig. 3. Moment 0 maps of the e8 region in 40 different lines over the range 52 to 63 km s⁻¹ with continuum subtraction using the 30th percentile emission over the ranges 25-40 and 75-90 km s⁻¹. All images are on the same scale, and the negative features show absorption against the continuum. As in e2, there is extended emission in the CH₃OH and OCS lines, but in contrast with e2, the other CH₃Ox lines are more compact. SO is brighter than OCS in e8, whereas the opposite is true in e2.

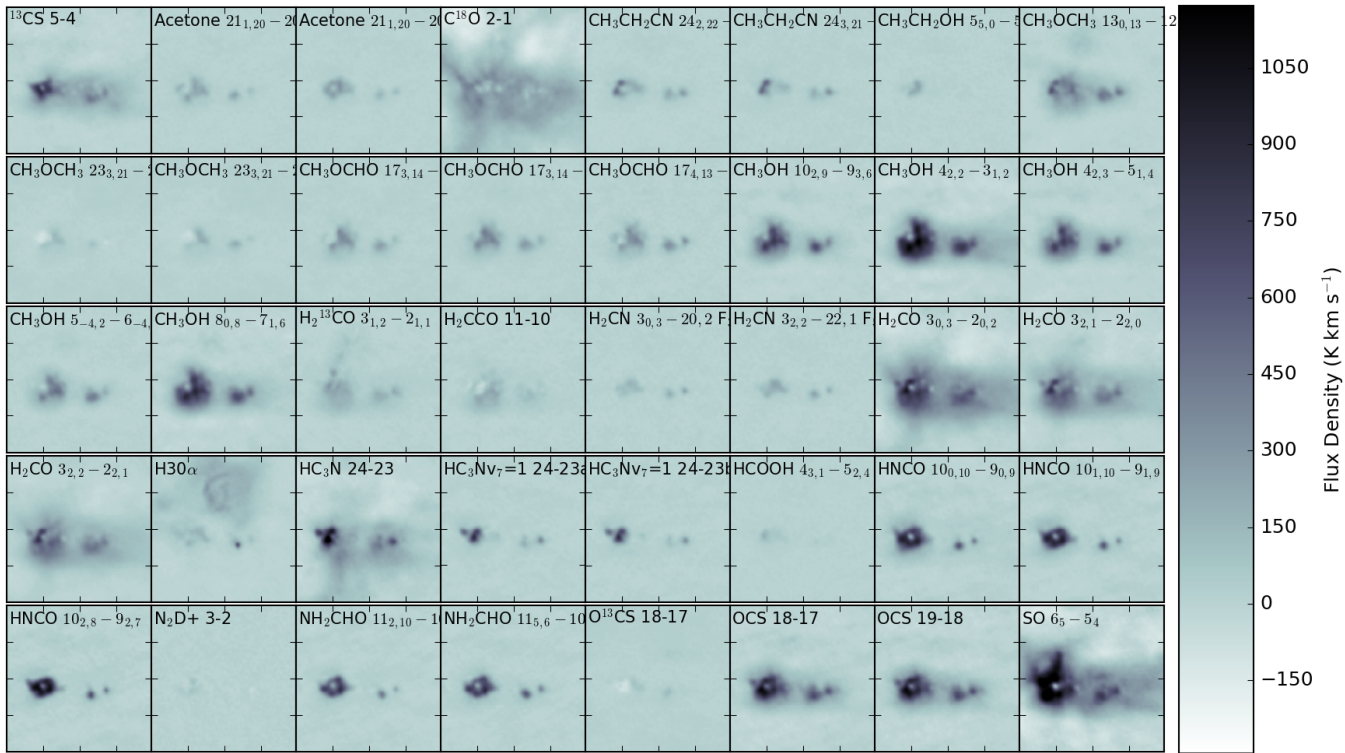


Fig. 4. Moment 0 maps of the W51 IRS2 region in 40 different lines over the range 54 to 64 km s⁻¹ with continuum subtraction using the 30th percentile emission over the ranges 25-40 and 75-90 km s⁻¹. All images are on the same scale, and the negative features show absorption against the continuum. Qualitatively, the relative extents of species seem comparable to e8. The H30 α point source is W51 d2.

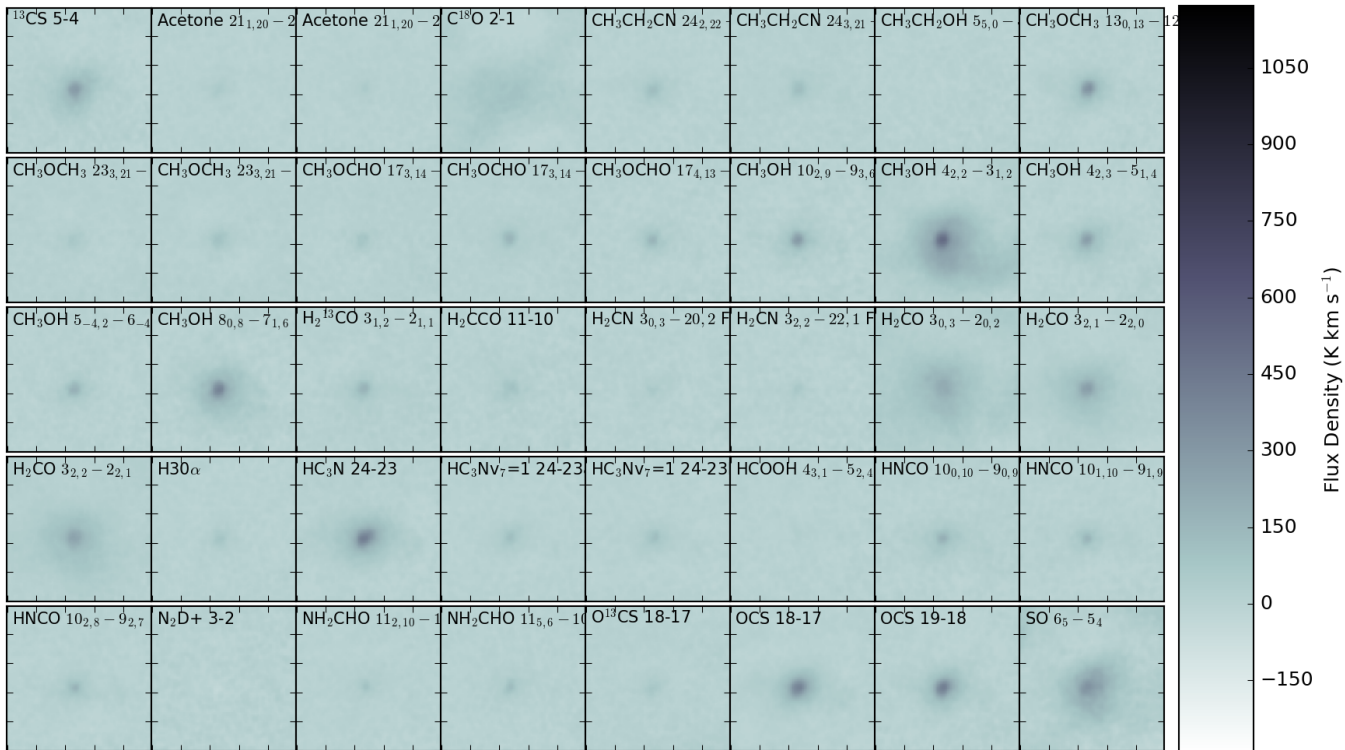


Fig. 5. Moment 0 maps of the ALMAMm14 region in 40 different lines over the range 58 to 67 km s⁻¹ with continuum subtraction using the 30th percentile emission over the ranges 25-40 and 75-90 km s⁻¹. All images are on the same scale. ALMAMm14 is one of the brightest sources outside of e2/e8/IRS2, but it is substantially fainter than those regions. Still, it has a noticeably rich chemistry.

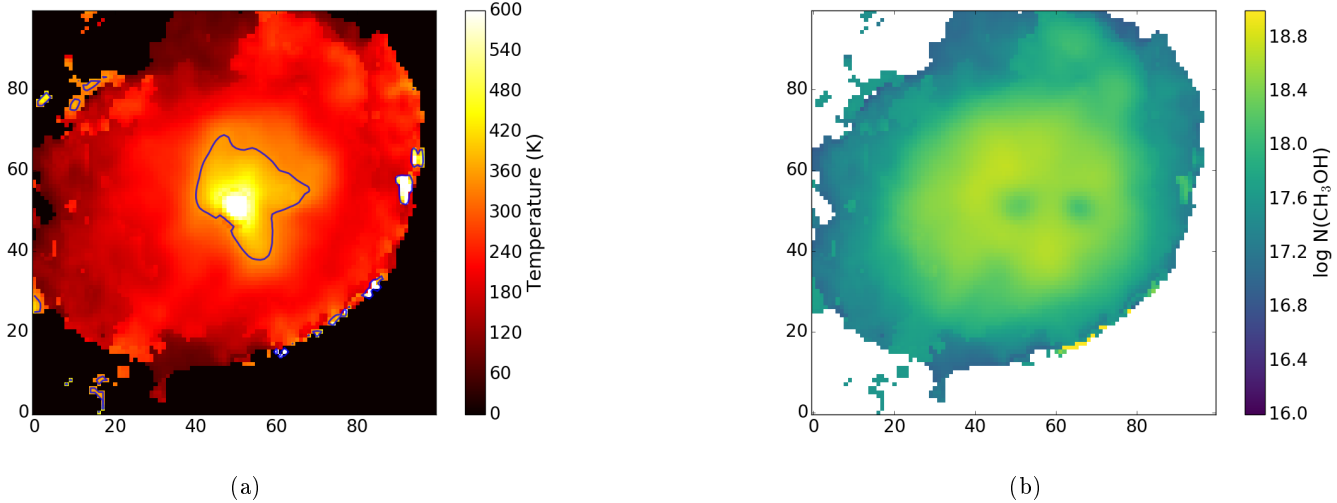


Fig. 6. Methanol temperature and column density maps around e2. The central regions around the cores appear to have lower column densities because the lines become optically thick and self-absorbed. The contour in the temperature map is at 350 K, where red meat is typically considered “well-done”.

The CH_3OH abundance is derived by comparing the rotational diagram (RTD) fitted CH_3OH column density to the dust column density while using the CH_3OH -derived temperature as the assumed dust temperature. The figure shows all pixels within a $3''$ (16200 AU) radius of e2e, with pixels having low column density and high temperature (i.e., pixels with bad fits) and those near e2w (which may be heated by a different source) excluded. We used moment-0 (integrated intensity) maps of the CH_3OH lines to perform these RTD fits, which means we have ignored the line profile entirely and in some cases underestimated the intensity of the optically thick lower-J lines: in the regions of highest column, the column is underestimated and the temperature is overestimated, as can be seen in Figure 8.

A few features illustrate the effects of thermal radiative feedback on the gas. The temperature jump starting inwards of $r \sim 1.5''$ (8100 AU; Figure 11b) is substantial, though the 100-200 K floor at greater radii is likely artificial as the low-J transitions are not consistent with a thermal distribution. There is an abundance enhancement at the inner radii, but it appears to be a radial bump rather than a pure increase. The abundance enhancement is probably real, and is approximately a factor of $\sim 5 - 10$. The inner abundance dip is caused by two coincident effects: first, the CH_3OH column becomes underestimated because the CH_3OH is self-absorbed, and second, the dust becomes optically thick, blocking additional CH_3OH emission, though this latter effect is somewhat self-regulating since it also decreases the dust column (the denominator in the abundance expression).

3.5. Radial mass profiles around the most massive cores

In Figure 12, we show the radial profiles extracted from the three high-mass protostellar cores in W51: W51 North, W51 e2e, and W51 e8. The plot shows the enclosed mass out to $\sim 1''$ (5400 AU). On larger spatial scales, the enclosed mass rises more shallowly, indicating the end of the core.

All three sources show similar radial profiles, containing up to $3000 M_\odot$ within a compact radius of 5400 AU (0.03 pc). However, the temperature structure within these sources is certainly not homogeneous, and likely a large fraction of the total flux comes from $T \gtrsim 300$ K heated material (Section C.3; Goddi et al. 2016). If the observed dust were all at 600 K, the mass would be $\sim 17\times$ lower, $100 M_\odot$, which we treat as a strict lower bound as it is unlikely that the dust at more than $r \gtrsim 1000$ AU is so warm. Additionally, it is likely that a substantial mass of cold dust is also present but undetectable because it is hidden by the hotter dust.

3.6. Ionizing vs non-ionizing radiation

The formed and forming protostars are producing a total $\gtrsim 10^7 L_\odot$ of far infrared illumination (Ginsburg et al. 2016b). This radiation heats the cloud’s molecular gas, affecting the initial conditions of future star formation.

The ionizing radiation in W51 was discussed in detail in Ginsburg et al. (2016b). Ionizing radiation affects much of the cloud volume, but little of the high-density prestellar material: there is no evidence of increased gas temperatures in the vicinity of H II regions. While in Section 3.3 we identify chemically enhanced regions as those where radiative feedback has heated the dust and released ices into the gas phase, no such regions are observed surrounding the compact H II regions.

The chemical maps shown in Section 3.3 show the volumes of gas clearly affected by newly-forming high-luminosity stars. The CH_3OH -enhanced region around W51e2e extends 0.04 pc, or 8500 AU (see Section 3.4). Other locally enhanced species, especially the nitrogenic molecules HNCO and NH_2CHO , occupy a smaller and more asymmetric region around e2e and e2w (Figure 14). These chemically enhanced regions are most prominent around the weakest radio sources or regions with no radio detection; they are most likely heated by direct infrared radiation from these sources.



Fig. 7. A sampling of fitted rotation diagrams of the detected CH₃OH transitions. These are meant to provide validation of the temperatures and column densities derived and shown in Figure 6. The lower-left corner shows the position from which the data were extracted in that figure in units of figure fraction. The horizontal black lines show the detection threshold of each of the transitions; points below these lines are ignored when fitting, and instead the threshold itself is used. The fitted temperature and column are shown in the top right of each plot.

3.7. Outflows

While many outflows were detected, we defer their discussion to Appendix B, as the details of these flows is not relevant to the main point of the paper. However, we note that out of the dozen or so outflows detected, *none* come from radio continuum sources (H II regions). All outflows that have a clear origin come from millimeter-detected, centimeter-faint sources, suggesting that these sources are accreting and are not emitting ionizing radiation.

4. Discussion

4.1. The scales and types of feedback

The most prominent features of our observations are the warm, chemically enhanced regions surrounding the high-

est dust concentrations, and the corresponding *lack* of such features around the ionized nebulae. This difference implies that the immediate star formation process - that of gas collapse and fragmentation from a molecular cloud - is primarily affected by feedback from stars that are presently accreting and therefore emitting most of their radiation in the infrared, *not* from previous generations of now-exposed stellar photospheres.

On the scales relevant to the fragmentation process, i.e., the ~ 0.1 pc scales of prestellar cores, this decoupling can be explained simply. Stellar light is produced mostly in the UV, optical, and near-infrared. As soon as a star is exposed, either by consuming or destroying its natal core, that light is able to stream to relatively large ($\gtrsim 1$ pc) scales before being absorbed. At that point, the stellar radiation is poorly coupled to the scales of direct star formation. By contrast,

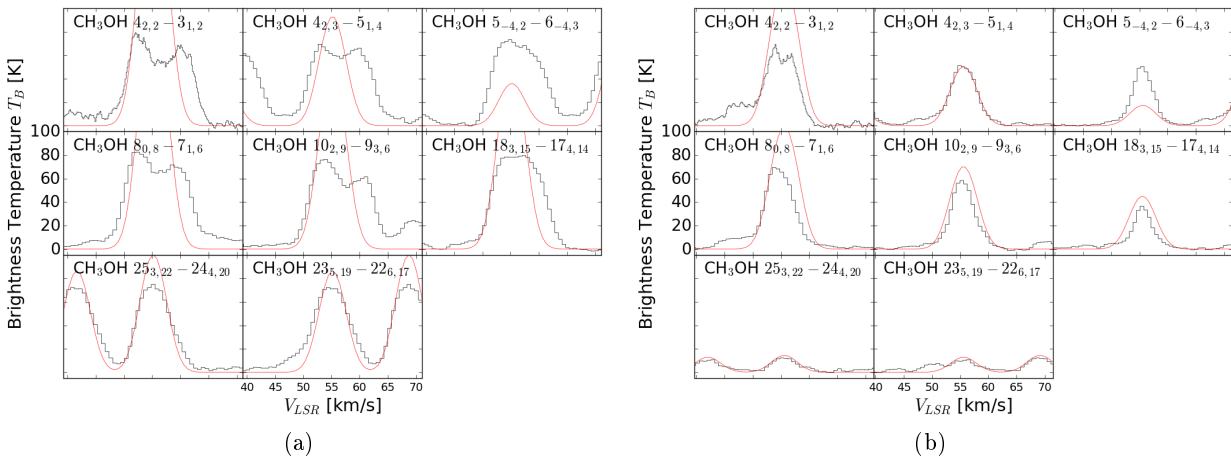


Fig. 8. Spectra of the CH_3OH lines toward a pair of selected pixels just outside of the e2e core. (a) is $0.55''$ and (b) is $1.33''$ from e2e. The red curves show the LTE model fitted from a rotational diagram as shown in Figure 7. The model is not a fit to the data shown, but is instead a single-component LTE model fit to the integrated intensity of the lines shown. As such, the fit is not convincing, and it is evident that a single-temperature, single-velocity model does not explain the observed lines. Nonetheless, a component with the modeled temperature is likely to be present in addition to a cooler component responsible for the self-absorption in the low- J lines. (a) shows a pixel close to the center of e2e, which is probably optically thick in most of the shown transitions, while (b) shows a better case where the highest- A_{ij} lines are overpredicted but many of the others are well-fit.

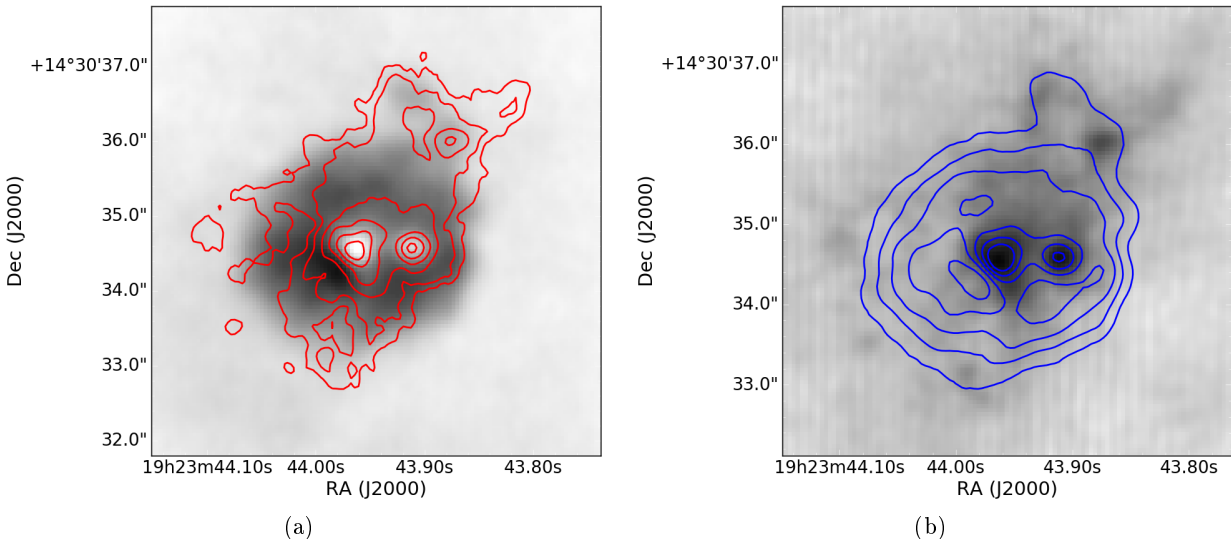


Fig. 9. Images showing CH_3OH $10_{2,9} - 9_{3,6}$ and 225 GHz continuum emission, with CH_3OH in grayscale and continuum in contours (left) and continuum in grayscale, CH_3OH in contours (right). The fainter (whiter) regions in the center of the CH_3OH map correspond to the bright continuum cores and show where all lines appear to be self-absorbed.

stars embedded in their natal cores will have all of their light reprocessed from UV/optical/NIR to the far-IR within a < 0.1 pc sphere, providing a far-infrared background light capable of heating its surroundings.

The different effects of ionizing vs thermal radiation can be seen directly in the three main massive star forming regions, e2, e8, and north. Figures 14 and 15 show both the highly-excited warm molecular gas in color and the free-free emission from ionized gas in contours. As described in Section 3.6, the spatial differences indicate that the ionizing radiation sources - the exposed OB stars - have little effect on the star-forming collapsing and fragmenting gas.

The low impact of photospheric radiation on collapsing gas suggests that second-generation star formation is relatively unaffected by its surroundings. Instead, the stars of

the same generation - those currently embedded and accreting - have the dominant regulating effect on the gas temperature. To the extent that gas temperature governs the IMF, then, the formation of the IMF *within clusters* is therefore predominantly self-regulated, with little external influence.

4.1.1. Hot core chemical structure

In Section 3.3, we showed regions with enhanced emission in a variety of complex chemical species over a large volume. While it is not generally correct to conclude that enhanced emission indicates enhanced abundance, the additional analysis of the CH_3OH abundance in Section 3.4

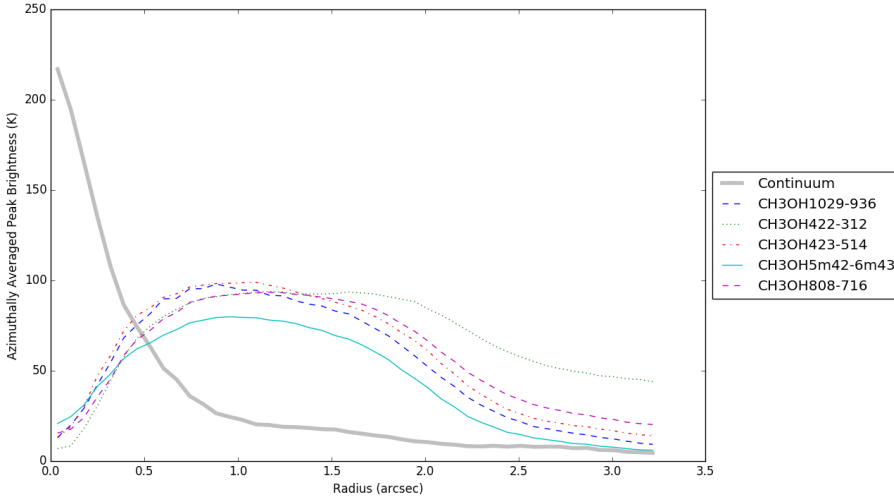


Fig. 10. Radial profiles of the peak surface brightness of five CH₃OH transitions along with the profile of the continuum brightness. The radial profiles were constructed from images with 0.2'' resolution including only 12m data. The central dip shows where the lines go into absorption, though they are only seen in absorption at $\sim 55 \text{ km s}^{-1}$. The CH₃OH lines are continuum-subtracted.

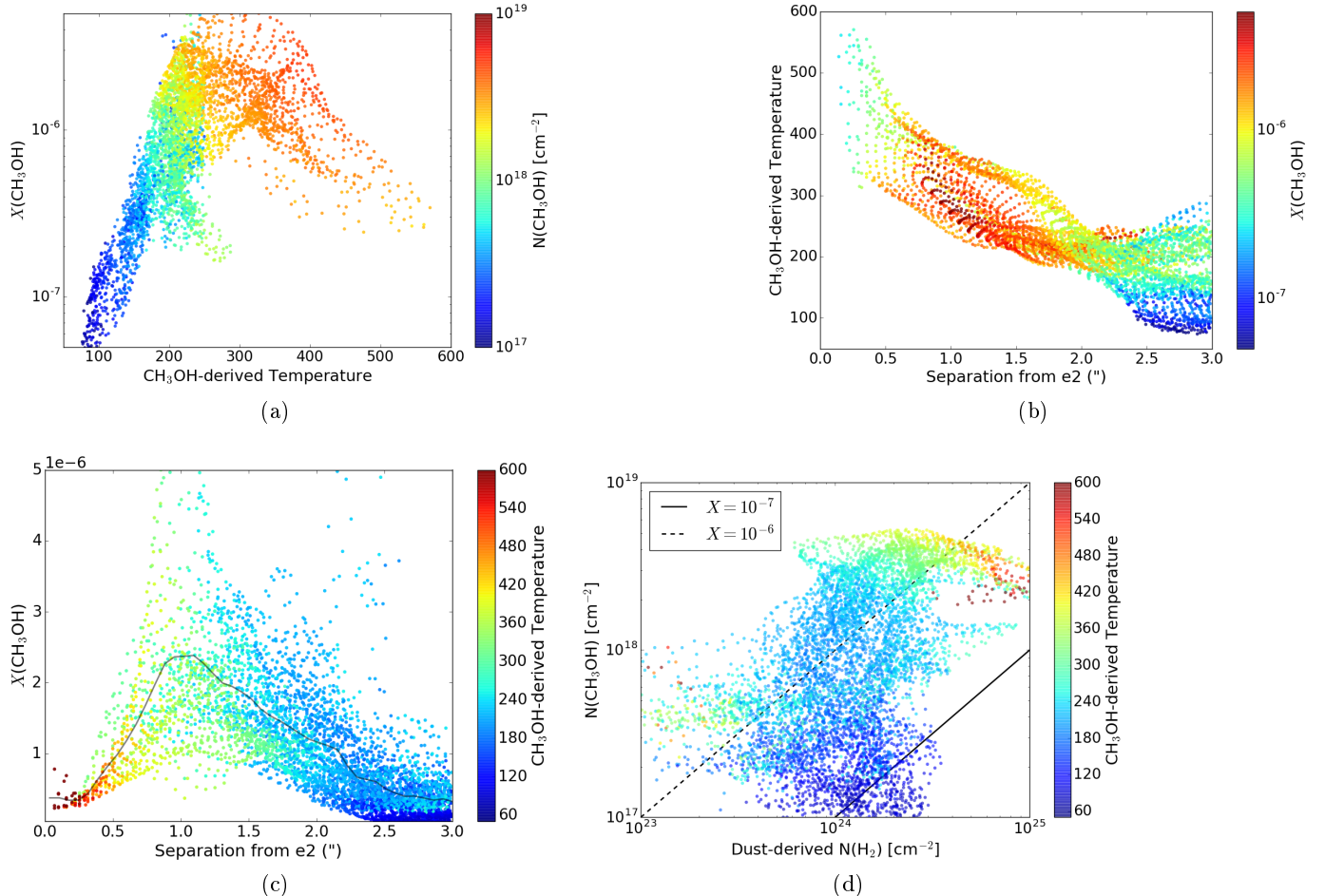


Fig. 11. Comparison of the CH₃OH temperature, column density, and abundance. (a) The relation between temperature and abundance. There is a weak correlation, but most of the high abundance regions are at high temperatures. (b) Temperature vs distance from e2e. There is a clear trend toward higher temperatures closer to the central source (c) Abundance vs distance from e2e. The apparent dip at $r < 1''$ is somewhat artificial, as it is driven by a rising dust emissivity that corresponds to an increasing optical depth in the dust. The CH₃OH column in this inner region is likely to be underestimated. (d) CH₃OH vs dust column density.

suggests that there is a genuine enhancement in complex chemical abundances toward these hot cores.

We have not performed a detailed abundance analysis of multiple species, but we nonetheless suggest that

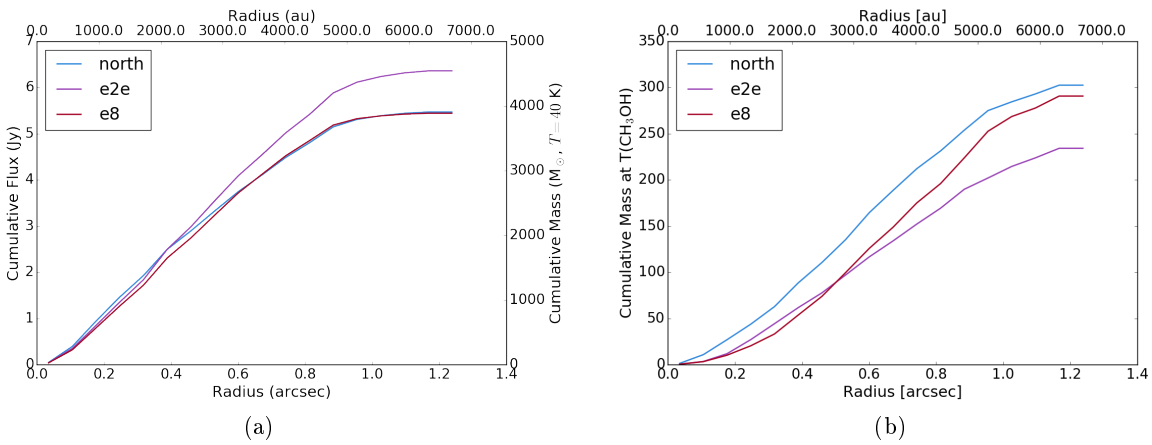


Fig. 12. The cumulative (a) flux density radial profile and (b) mass radial profile centered on three massive protostellar cores. They share similar profiles and are likely dominated by hot dust in their innermost regions, but they are more likely to be dominated by cooler dust in their outer, more massive regions. The cumulative mass distribution may therefore be deceptive. In (a), we use a constant temperature to convert from flux to mass. In (b), we use the temperature map computed from CH_3OH in Section 3.4.

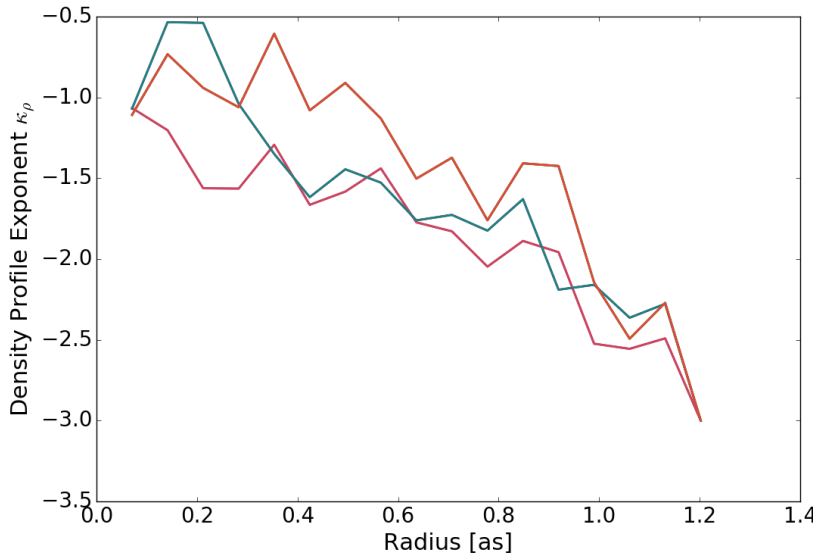


Fig. 13. The radial mass profile exponent κ_ρ as a function of radius. The ‘fiducial value’ used in the McKee & Tan (2003) model is $\kappa_\rho = 1.5$, but importantly it is *constant* at $t = 0$. A non-constant κ_ρ indicates that collapse is not self-similar, and the flattening toward smaller radii suggests that it is slower than freefall collapse.

these sharp-edged bubbles around the hot cores represent sublimation zones in which substantial quantities of grain-processed materials are released into the gas phase. The relatively sharp edges likely reflect the particular point where the temperature exceeds the sublimation temperature for each species (Garrod et al. 2006), though some species may appear at temperatures above or below their sublimation temperature if they are mixed into ices that have a different sublimation temperature.

Most of the lines identified in the hot cores e2e, e8, and north are also present in ALMAmm14. However, their extent is greater toward the more luminous sources. An examination of the relationship between the luminosity of the protostars and the extent of their chemically enhanced zones will be useful for identifying further very massive protostars.

4.1.2. Outflows

While the outflows described in Section B are impressive and plentiful, they are obviously not the dominant form of feedback, as their area filling factor is small compared to that of the various forms of radiative feedback. A low area filling factor implies a substantially smaller volume filling factor and therefore a lower overall effect on the cloud. However, these outflows likely do punch holes through protostellar envelopes and the surrounding cloud material, allowing radiation to escape.

The detection of widespread high-J CH_3OH emission around the highest-mass protostars suggests that the use of CH_3OH as a bulk outflow tracer as suggested by Kristensen & Bergin (2015) is not viable in regions with forming high-mass stars. While mid-J CH_3OH emission is detected associated with the outflow (e.g., the J=10-9 transition), it

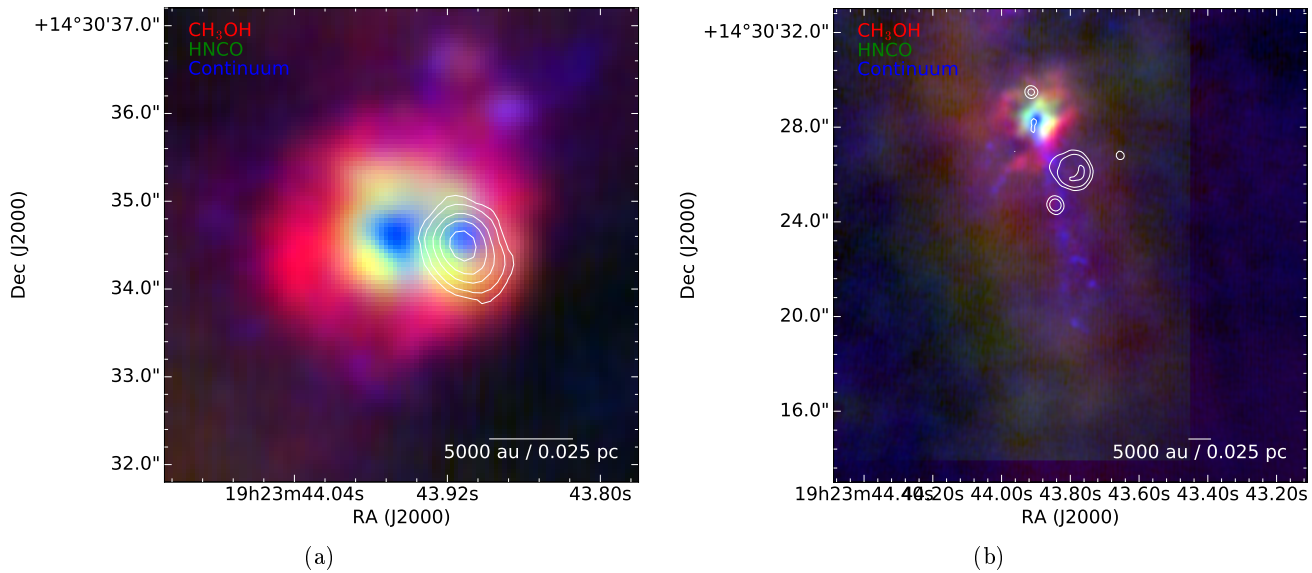


Fig. 14. Image of CH_3OH $8_{0,8} - 7_{1,6}$ (red), HCNO $10_{0,10} - 9_{0,9}$ (green), and 225 GHz continuum (blue) toward (a) W51e2 (b) W51e8. The contours show Ku-band radio continuum emission tracing the H II regions (a) W51 e2w and (b) W51 e1, e3, e4, e9, and e10. The CH_3OH emission is relatively symmetric around the high-mass protostar W51 e2e and the weak radio source W51 e8, suggesting that these forming stars are responsible for heating their surroundings. By contrast, the H II regions do not exhibit any local molecular brightness enhancements (except e8), indicating that the H II regions are not heating their local dense molecular gas.

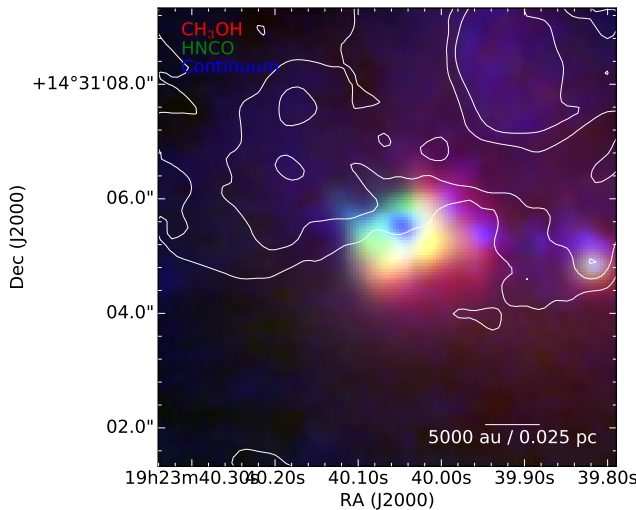


Fig. 15. Image of CH_3OH $8_{0,8} - 7_{1,6}$ (red), HCNO $10_{0,10} - 9_{0,9}$ (green), and 225 GHz continuum (blue) toward north, as in Figure 14. The contours show Ku-band radio continuum emission tracing the diffuse IRS 2 H II region.

is completely dominated by the general ‘extended hot core’ emission described in Section 3.3.

None of the outflows initiate in UCH_{II} or HCH_{II} regions. While a clear origin cannot be determined for all of the outflows, it is clear that no cm continuum sources lay at the base of any. The lack of molecular outflows toward these sources implies that they are accreting at most weakly or are accreting (and ejecting) only atomic or ionized material.

4.2. The accreting phase of high-mass star formation

The strong outflows observed around the highest-mass forming stars, e2e, e8, and north are clear indications of ongoing accretion onto these sources. However, the bright

H II regions, including e2w, e1, and d2, all lack any sign of an outflow or a surrounding rotating molecular structure. Most of these sources lack any surrounding molecular material at all.

Some models of high-mass star formation suggest that accretion continues through the ionized (H II region) phase (e.g. Keto 2007). The lack of molecular material around the majority of the compact H II regions in W51 suggests instead that most of the accretion is done by the time an H II region ignites.

There is one counterexample in our sample. The source d2 is a bright, compact H II region, but it is also surrounded by a molecular enhancement. However, it does not appear to drive an outflow, so there is again no direct evidence of ongoing accretion.

The correlation of the extended hot cores with outflow-driving source suggests that the heating of these hot cores is either from accretion luminosity, or that the high accretion rate indicated by the presence of outflows is necessary to reprocess stellar photospheric light into the infrared.

4.3. The accreting stars

In Sections ?? and 3.1.2, we noted that the *lower limit* luminosities for the three most massive cores correspond to early B-type photospheres. Such stars should emit enough radiation to ignite luminous compact H II regions. The upper limits on the presence of such an H II region are constraining, with $R < 100 \text{ AU}$, which is consistent with the presence of these stars, but inconsistent with any hotter or more luminous (spectral type $< \text{B}0.5\text{V}$). If the stellar luminosities are an order of magnitude or more higher, which is possible given the low-resolution constraints on the bolometric luminosity (Ginsburg et al. 2016a; Sievers et al. 1991) and likely if a large fraction of the stellar radiation is escaping along outflow cavities (Kuiper & Yorke 2012; Zhang et al. 2013), the luminosity would be too large and the UV radiation too small to be consistent with a main-sequence OB star.

Since we can provide only upper limits on the UV radiation, it is possible that there is none at all. The very large mass reservoir suggests that high accretion rates are possible, and the bright molecular outflows show that accretion is proceeding vigorously (though we have not quantified the rate). Rapid accretion, and in particular rapid and *variable* accretion, can change the properties of the underlying star, bloating the star and reducing its effective photospheric temperature (Hosokawa & Omukai 2009; Smith et al. 2012; Hosokawa et al. 2016). Such stars can achieve radii $R \gtrsim 200R_{\odot} \sim 1 \text{ AU}$ while retaining photospheric temperatures $T \lesssim 5000 \text{ K}$. **We hope to explore this possibility further in a subsequent paper.**

4.4. Fragmentation: Jeans analysis

Fragmentation is one of the critical problems in high-mass star formation. Assuming typical initial conditions for molecular clouds, with temperatures of order 10 K, gas is expected to fragment into sub-solar mass cores, preventing material from accreting onto single high-mass stars (Krumholz et al. 2015). Even after high-mass stars successfully form, further fragmentation could halt the growth of these stars and limit their final mass (Peters et al. 2010b).

Thermal Jeans fragmentation can be limited or suppressed entirely if the gas is warm enough. The high observed gas temperatures, $T \sim 100 - 600 \text{ K}$ over $\sim 10^4 \text{ AU}$, around the high mass protostars indicate that their radiative feedback in the infrared has a dramatic effect on the gas. The heated region qualitatively matches that of Krumholz (2006), who described a core heated only by accretion luminosity down to $R = 10 \text{ AU}$ and therefore gave a lower limit on the total heating.

We examined the temperature structure around the highest-mass cores in Section C.3 and the mass structure in Section 3.5. We put these together to measure the Jeans mass, $M_J = (\pi/6)c_s^3 G^{-3/2} \rho^{-1/2}$, and length, $\lambda_J = c_s G^{-1/2} \rho^{-1/2}$. **Anyone have strong opinions about the leading numerical constants?, in Figure 16.** The Jeans

length is comparable to the hot core size, so no fragmentation should be occurring. Additionally, the Jeans mass is anywhere from 3-10× higher than the (mass-weighted) peak of the stellar initial mass function (IMF), $M_{peak} \approx 0.4 M_{\odot}$, at most radii. The core is therefore ~ 100 Jeans masses, but stable against further fragmentation.

The high gas temperature therefore provides a mechanism for MYSOs to avoid the “fragmentation-induced starvation” problem discussed by Peters et al. (2010b,a); Girichidis et al. (2012). Apparently, stars above some mass are able to heat hundreds of M_{\odot} of material surrounding them to such a degree that it cannot fragment further, providing an enormous reservoir to feed from.

Within this large reservoir, there are few currently-detected fragments. In our data, within 6500 AU of W51 north, there is only 1 (ALMamm35), around e2e there is the HII region e2w and possibly 2-3 others between 5000 and 6500 AU, and around e8 there are none. Admittedly, our data are not very sensitive in the areas immediately surrounding these cores because of dynamic range limitations, but the higher Jeans mass noted above suggests that any fragments that do exist should be more massive and therefore more detectable.

Further fragmentation below 1000 AU is possible, e.g., as seen in NGC 6334Imm1 (Brogan et al. 2016). However, in the long baseline data to be presented in a future work (Goddi et al, in prep), very little additional fragmentation is observed. A few more sources are detected toward e2e and north and many toward e8, but the nature of those more compact ($< 200 \text{ AU}$) sources suggests they are protostellar or stellar. Additionally, unlike the centrally-clustered fragmentation seen in NGC 6334Imm1, the fragments that are detected appear spread out in W51.

By suppressing fragmentation in their surroundings, accreting massive stars are able to sustain their mass reservoir. They effectively create their own cores. Given the current structure of the observed cores and their marginal stability against fragmentation, it is unlikely that these cores could have existed at all without the presence of a central heating source. Should these $> 200 M_{\odot}$ cores have been present before high-mass star formation initiated, resting at $T \sim 20 \text{ K}$ as in a typical molecular cloud, they would have been subject to Jeans fragmentation on a much smaller scale and would have formed a cluster of smaller stars. This implies that the mass currently in the core had to be assembled from larger scales while suppressing or slowing collapse on smaller scales, which is essentially the opposite of inside-out collapse.

4.5. High-mass star formation within dense protoclusters

Since massive ($M \gtrsim 250 M_{\odot}$) hot cores presently exist, and they appear to be the precursors to a next generation of high mass stars, there is a clear route to high-mass star formation given the presence of strong feedback sources. However, this raises the question of what the initial conditions were. Did the current generation of forming massive stars start life the same way as previous generations?

One possibility hinted at by the density of hyper- and ultra-compact H II regions around each of the massive cores is that they did not. Heating from previous generations of moderate mass stars could have warmed the gas, suppressing fragmentation into the sub-solar mass objects typical in local clouds until enough gas was present to collapse into

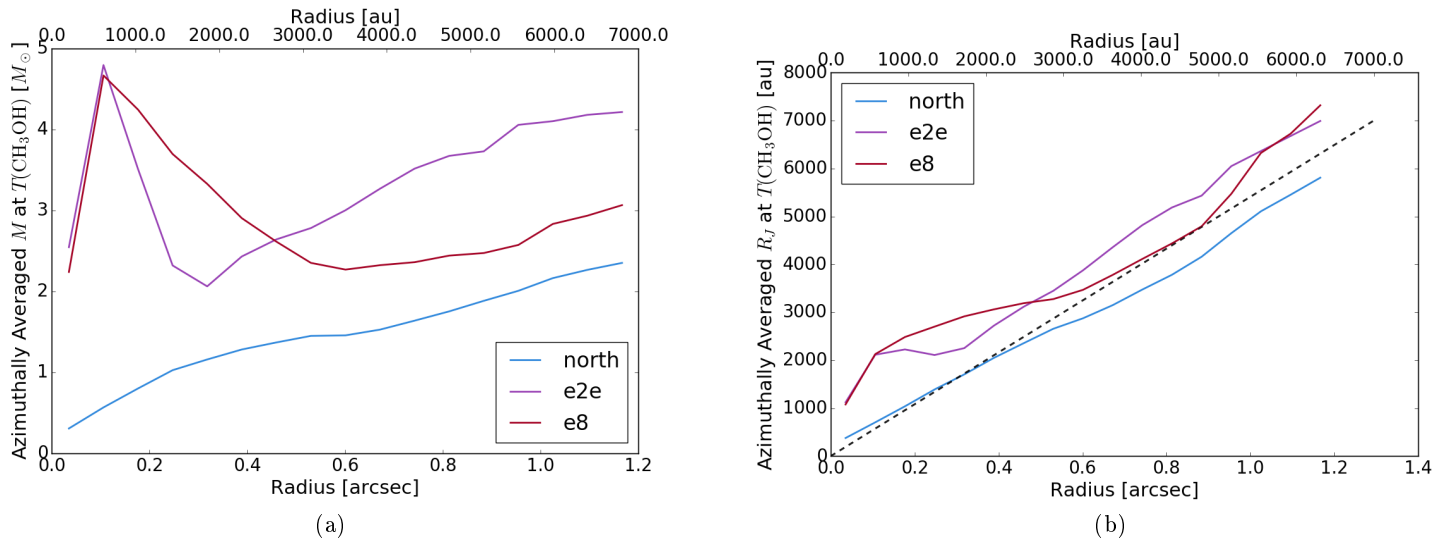


Fig. 16. The azimuthally averaged (a) Jeans mass and (b) Jeans length surrounding the three most massive cores. We used the CH₃OH temperature from 3.4, Figure 12b in both the Jeans mass calculation and the dust-based mass determination. The density used for the mass calculation is assumed to be distributed over spherical shells. In (b), the dashed black line shows the $R_J = R$ line. When $R_J > R$, the gas is on average stable against fragmentation on the measured length scale. Since the medium is clearly *not* isothermal or uniform density, though, this only shows a rough approximation of the stability.

a substantially larger object. This toy model is analogous to the ‘cooperative accretion’ mode suggested by Zinnecker & Yorke (2007), but at a much earlier stage in the cluster development when the gas is still molecular and dusty and therefore capable of efficient cooling. It is also similar to the results of Krumholz et al. (2011), in which radiative heating drove up the peak of the IMF; in this case, though, we suggest that the affected region is smaller (not the whole cloud) and that the “top-heavy IMF” is a solution, not a problem.

In this scenario, the highest mass stars (probably “very massive stars”, $M \gtrsim 50 M_{\odot}$) would only be capable of forming within dense, clustered environments, since larger stars would be prevented from forming by earlier fragmentation elsewhere. The IMF would then be built up by an inverse hierarchy, with progressively larger stars capable of forming over time until the gas is either exhausted (Ginsburg et al. 2016b) or expelled.

However, some of the assumptions in this scenario contradict our observations. If the previous generation were responsible for substantial gas heating, we might expect to see warm gas surrounding the HCH II regions. Instead, we see these stars barely interacting with the dense gas. However, it is possible that these stars are only effective at dense gas heating *before* they ignite Lyman continuum emission and blow out cavities, and afterward they are merely uninteracting witnesses to continued collapse.

The alternatives to this hypothesis are that the initial conditions were entirely set within the gas on these current scales, which seems implausible, or that the current high density of main-sequence stars (i.e., the observed HCH II regions) originated from a broader, lower-density distribution and dynamically collapsed into their current clustered state. If the stars illuminating HCH II regions formed somewhat earlier in a more distributed manner and fell into a common central potential, they would have had little effect on the dense gas temperature.

4.6. Comparison to high-mass star formation theories

Two general classes of star formation theory, “competitive accretion” and “turbulent core accretion” have dominated the discussion of high-mass star formation, though they are not fully complementary theories (Schilke 2016). In their extreme forms, they can be simplified to uniform seeds accreting different amounts of material over their lifetime in the case of competitive accretion and a single, initial, quasistatic high-mass gas core collapsing into a star in the case of turbulent core accretion.

Our observations of high-mass hot cores extending to radii ~ 5000 AU do not directly contradict either of these extremes, but instead suggests that the accretion models used within these theories must be modified.

If there are many simultaneously formed low-mass fragments competing for material, as in competitive accretion, it appears that the formation of a dominant most massive star dramatically changes the conditions for accretion. This single central source heats material enough to reduce the efficiency of Bondi-Hoyle accretion by a factor of 10 for a stationary object, though the reduction is negligible for an object moving near the Virial velocity ($v_{vir} \gtrsim 5 \text{ km s}^{-1}$ within the hot cores). However, this extended warm region suppresses the formation of new small fragments, as has been observed in simulations with much weaker feedback (e.g. Bate 2009). It is not clear whether the mass accumulated around the most massive protostars at present came from large radii, as in Smith et al. (2009), but it is certainly possible.

If the turbulent core model is used to describe these sources, a few obvious issues arise. First, the core structure is not a simple power-law with $\kappa_{\rho} = 1.5$, as usually assumed (McKee & Tan 2003; Zhang & Tan 2011). Figure 13 shows instead that the core is internally flatter and externally steeper than this assumption. Of course, the observations do not correspond to the initial conditions, so this comparison could more fairly be made with a later ‘snapshot’ from those models. Second, the more sophisti-

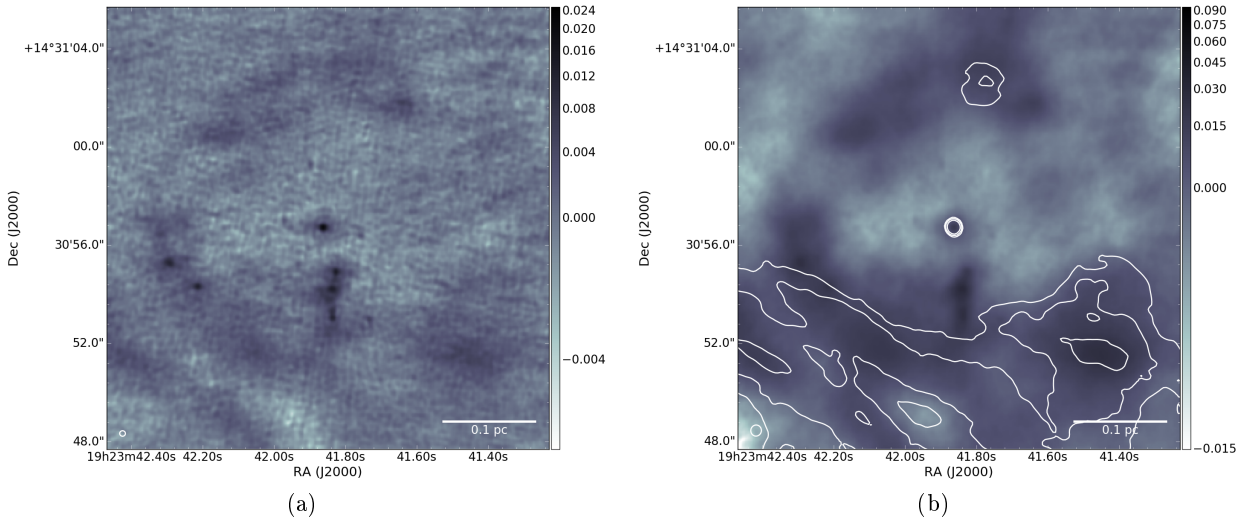


Fig. A.1. The bubble around source e5. The bubble interior shows no sign of centimeter emission, though the lower-left region of the shell - just south of the “cores” - coincides with part of the W51 Main ionized shell. The source of the ionization is not obvious. (*Left*): A robust -2.0 image with a small ($0.2''$) beam and poor recovery of large angular scale emission. This image highlights the presence of protostellar cores on the left edge of the bubble and along a filament just south of the central source. (*Right*): A robust +2.0 image with a larger ($0.4''$) beam and better recovery of large angular scales. The contours show radio continuum (14.5 GHz) emission at 1.5, 3, and 6 mJy/beam. While some of the detected 1.4 mm emission in the south could be free-free emission, the eastern and northern parts of the shell show no emission down to the $50 \mu\text{Jy}$ noise level of the Ku-band map, confirming that they consist only of dust emission.

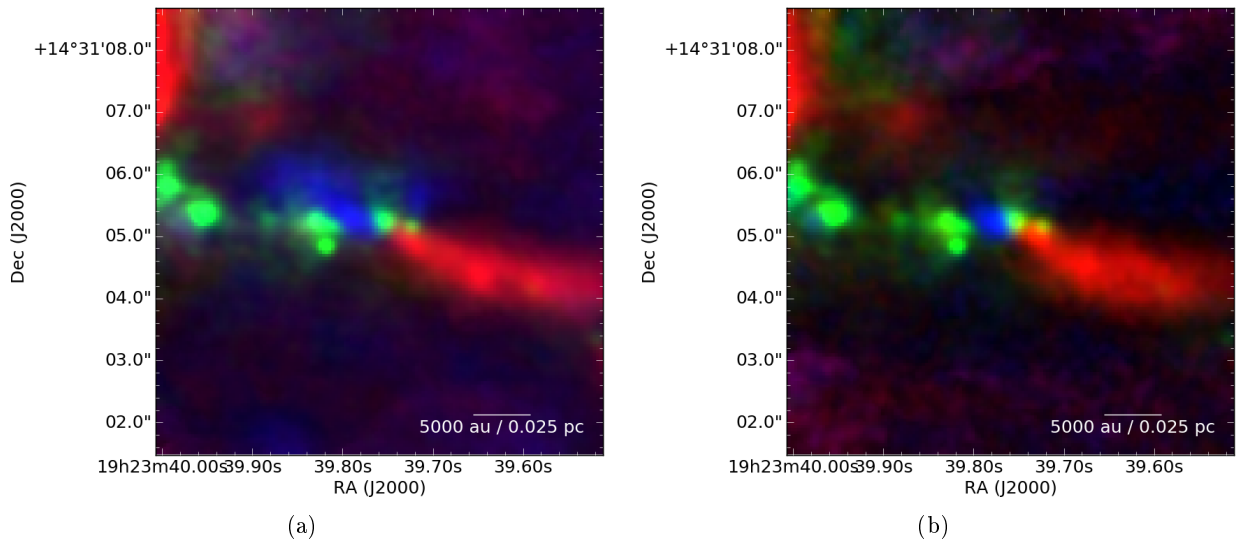


Fig. B.1. Outflows shown in red and blue for (a) CO 2-1 and (b) SO $65 - 54$ with continuum in green. This symmetric molecular outflow forms the base of the Lacy et al. (2007) ionized outflow detected further to the east. The continuum source is offset from the line joining the red and blue outflow lobes.

ure B.4). In the northwest, the redshifted part of this flow ($70 < v_{\text{LSR}} < 120 \text{ km s}^{-1}$) apparently collides with a blueshifted flow from another source ($22 < v_{\text{LSR}} < 45 \text{ km s}^{-1}$), suggesting that these outflows intersect, though such a scenario seems implausible given their small volume filling factor.

The extreme velocity and morphology carry a few implications for the accretion process in W51. The sharp symmetric truncation, combined with the extraordinary velocity, suggests that the outflow is freshly carving a cavity in the surrounding dense gas. The observed velocities are high enough that their bow shocks likely dissociated all

molecules, so some ionized gas is likely present at the endpoints; this ionized gas has not been detected in radio images because of the nearby 100 mJy HCHII region e2w. The dynamical age of the outflow is ~ 600 years at the peak observed velocity, which is a lower limit on the true age of the outflow.

Appendix B.0.4: e8

There are at least four distinct outflows coming from the e8 filament. The e8 core is launching a redshifted outflow to the northwest. A blueshifted outflow is coming from some-

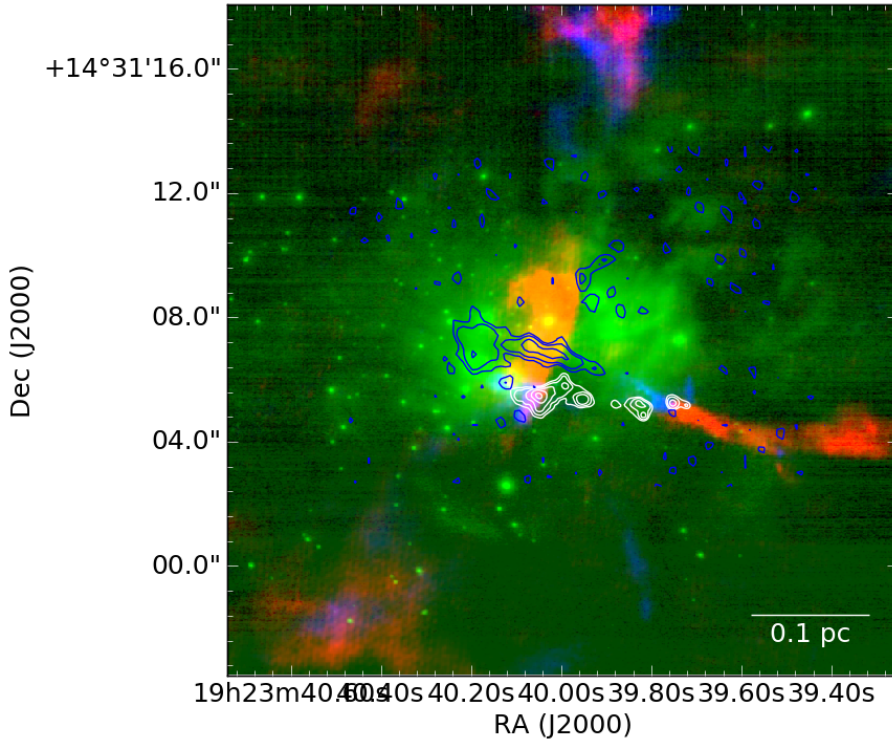


Fig. B.2. Outflows in the W51 IRS2 region. The green emission is NACO K-band continuum (Barbosa et al. 2008), with ALMA 1.4 mm continuum contours in white and H77 α contours in blue. The Lacy et al. (2007) jet is prominent in H77 α .

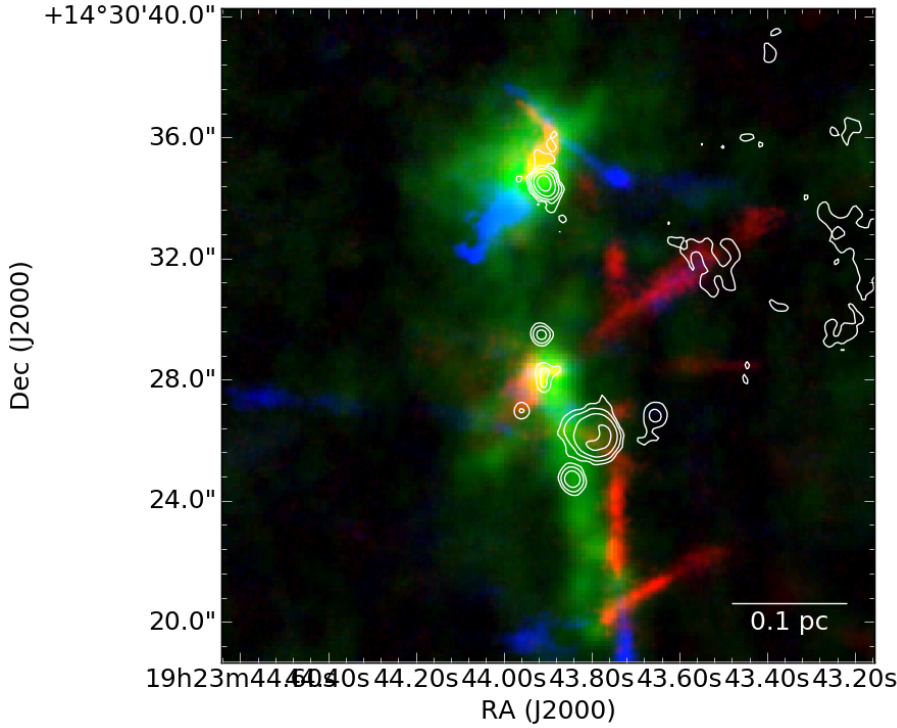


Fig. B.3. Outflows in red and blue overlaid on mm continuum in green with cm continuum contours in white. The northern source is e2, the southern source at the tip of the long continuum filament is e8.

where south of the e8 peak and pointing straight east. While these originate quite near each other, they seem not to have a common source, since the red and blue streams are not parallel (Figures B.3 and B.5). The e8 outflows are too confused and asymmetric for simple interpretation.

Appendix C: Details of the extracted sources

We provide additional information and details about the continuum source extraction, along with complete catalogs, in this Appendix.

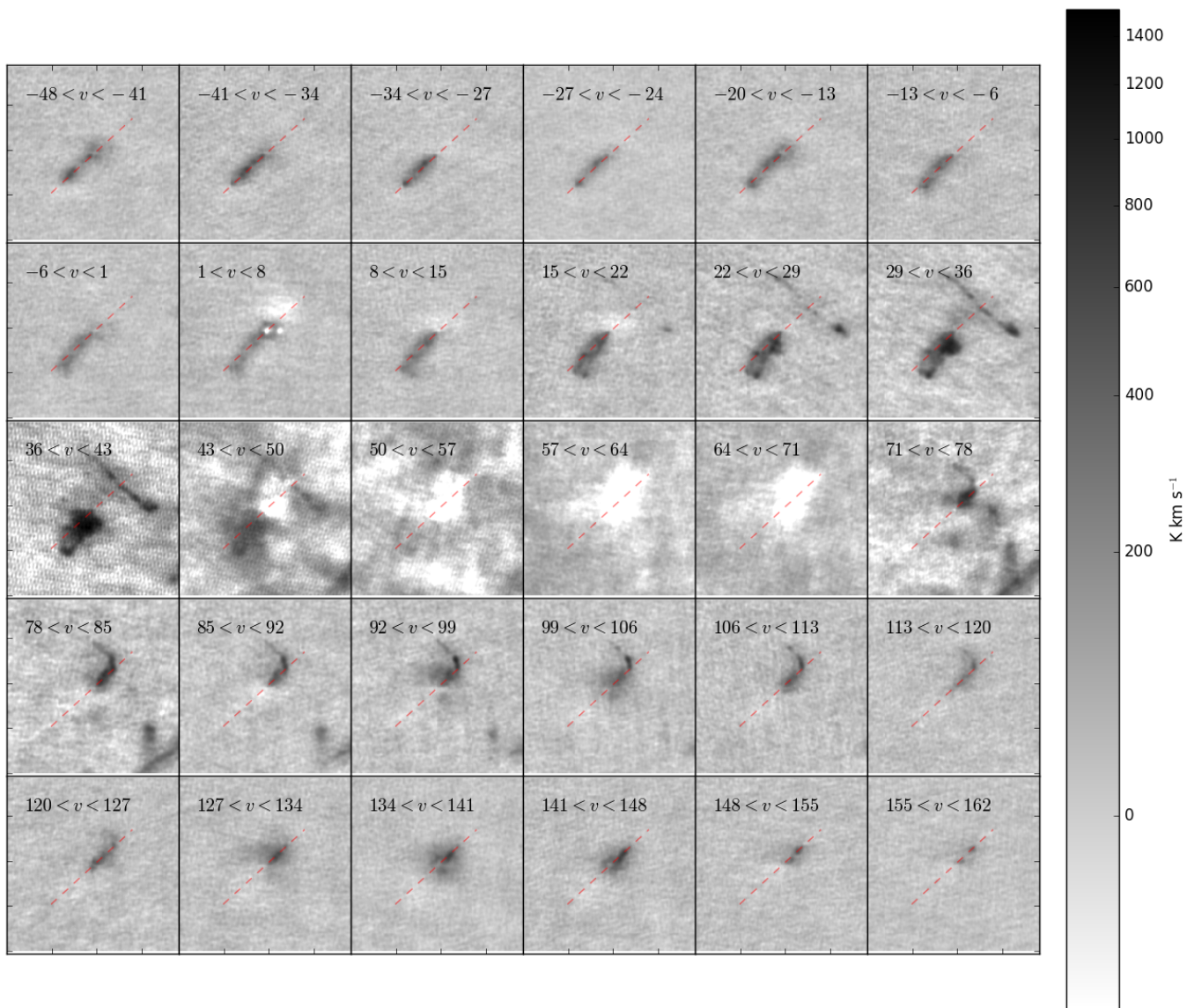


Fig. B.4. Channel maps of the e2e outflow in CO 2-1. The dashed line approximately connects the northwest and southeast extrema of the flow.

Appendix C.1: The spatial distribution of continuum sources

The detected continuum sources are not uniformly distributed across the observed region. The most notable feature in the spatial distribution is their alignment: most continuum sources collect along approximately linear features. This is especially evident in W51 IRS2, where the core density is very high and there is virtually no deviation from the line. The e8 filament is also notably linear, though there are a few sources detected just off the filament.

On a larger scale, the e8 filament points toward e2, apparently tracing a slightly longer filamentary structure. With some imagination, this might be extended along the entire northeast ridge to eventually connect in a broad half-circle with the IRS2 filament (Figure C.1). This morphology hints at a possible sequential star formation event, where some central bubble has swept gas into these filaments. However, this ring has no counterparts in ionized gas, and there is little reason to expect such circular symmetry from a real cloud, so the star forming circle may be merely a figment.

Whether it is physical or not, there is a notable lack of continuum sources within the circle. There is no lack of molecular gas, however, as both CO and H₂CO emission fill the full field of view.

Appendix C.2: Photometry

We created a catalog of the hand-extracted sources including their peak and mean flux density, their centroid, and their geometric properties. For each source, we further extracted aperture photometry around the centroid in 6 apertures: 0.2, 0.4, 0.6, 0.8, 1.0, and 1.5''. We performed the same aperture photometry on the W51 Ku-band images from [Ginsburg et al. \(2016a\)](#) to estimate the free-free contribution to the observed flux density measurements. These measurements are reported in Table C.2.

The source flux density distribution is shown in Figure C.2. The most common nearest-neighbor separation between cataloged sources is $\sim 0.3''$, which implies that the larger apertures double-count some pixels. The small-

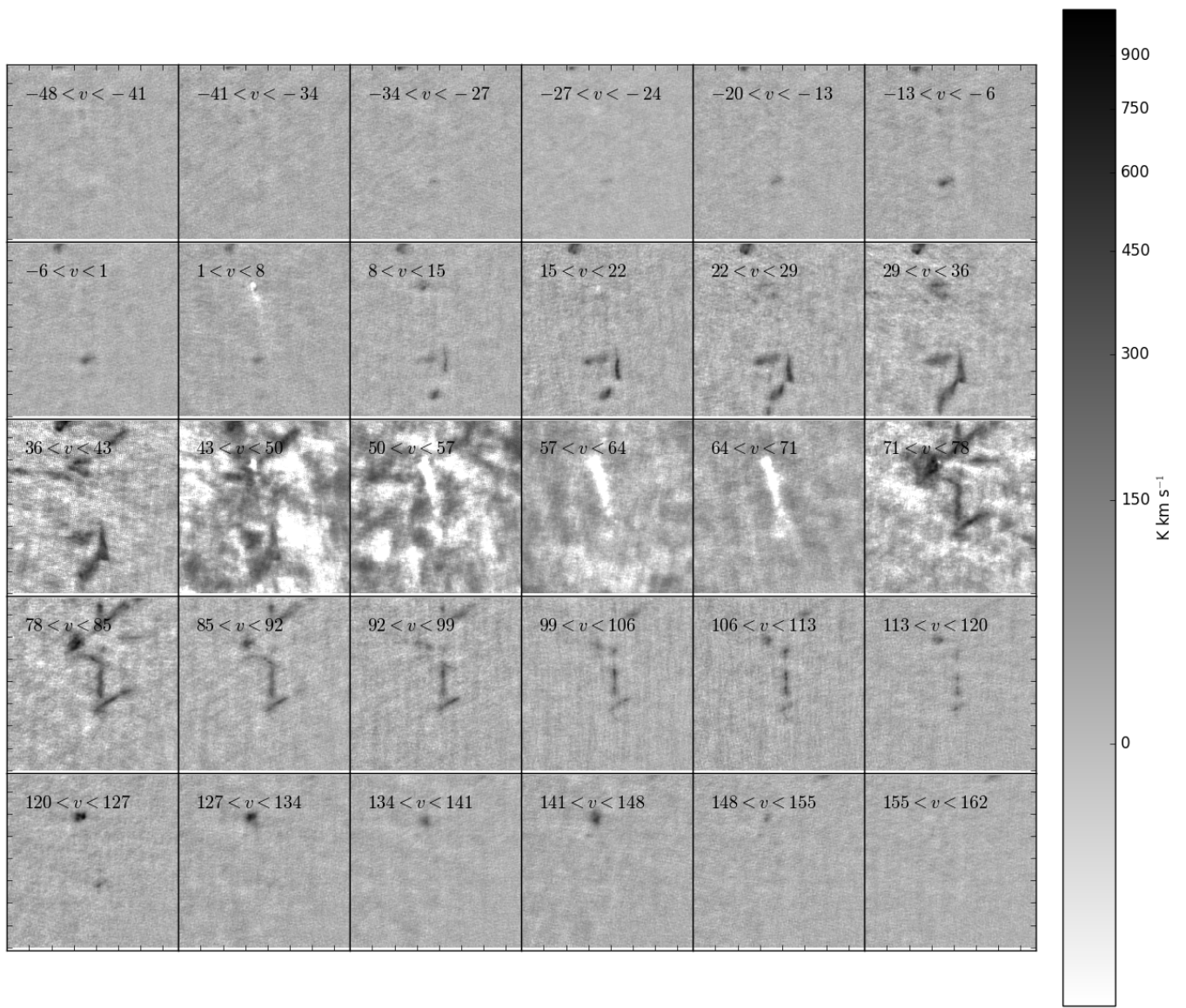


Fig. B.5. Channel maps of the e8 outflow in ^{12}CO 2-1. The outflows here are more erratic, with fewer clearly-connected red and blue lobes.

est separation is $0.26''$, so the $0.2''$ aperture contains almost only unique pixels. The corresponding masses are shown in Figure C.5 assuming the dust temperature is equal to the source's peak line brightness temperature (Section C.3).

Except where noted below, the hand-selected sources are used for further analysis as they are more reliable.

Appendix C.3: Temperature estimation of the continuum sources

The temperature is a critical ingredient for determining the total mass of each continuum source or region. Since we do not have any means of directly determining the dust temperature, as the SED peak is well into the THz regime and inaccessible with any existing instruments at the requisite resolution, we employ alternative indicators. Above a density $n \gtrsim 10^5 - 10^6 \text{ cm}^{-3}$, the gas and dust become strongly collisionally coupled, meaning the gas temperature should accurately reflect the dust temperature. Below this density, the two may be decoupled.

The average dust temperature, as estimated from Herschel Hi-Gal SED fits (Molinari et al. 2016; Wang et al. 2015), is 38 K when including the $70 \mu\text{m}$ data or 26 K when excluding it. This average is obtained over a $\sim 45''$ ($\sim 1 \text{ pc}$) beam and therefore is likely to be strongly biased toward the hottest dust in the HII regions. Despite these uncertainties, this bulk measurement provides us with a reasonable range to assume for the uncoupled, low-density dust, which (weakly) dominates the mass (see Section 3.2).

One constraint on the dust temperature we can employ is the absolute surface brightness. For some regions, especially the e8 filament and the hot cores, the surface brightness is substantially brighter than is possible for a beam-filling, optically thick blackbody at 20 K, providing a lower limit on the dust temperature ranging from 20 K (35 mJy/beam) to $\sim 300 \text{ K}$ (0.5 Jy/beam). Toward most of this emission, optically-thick free-free emission can be strongly ruled out as the driving mechanism using existing data that limits the free-free contribution to be $< 50\%$ if it is optically thick, and negligible ($<< 1\%$) if it is optically

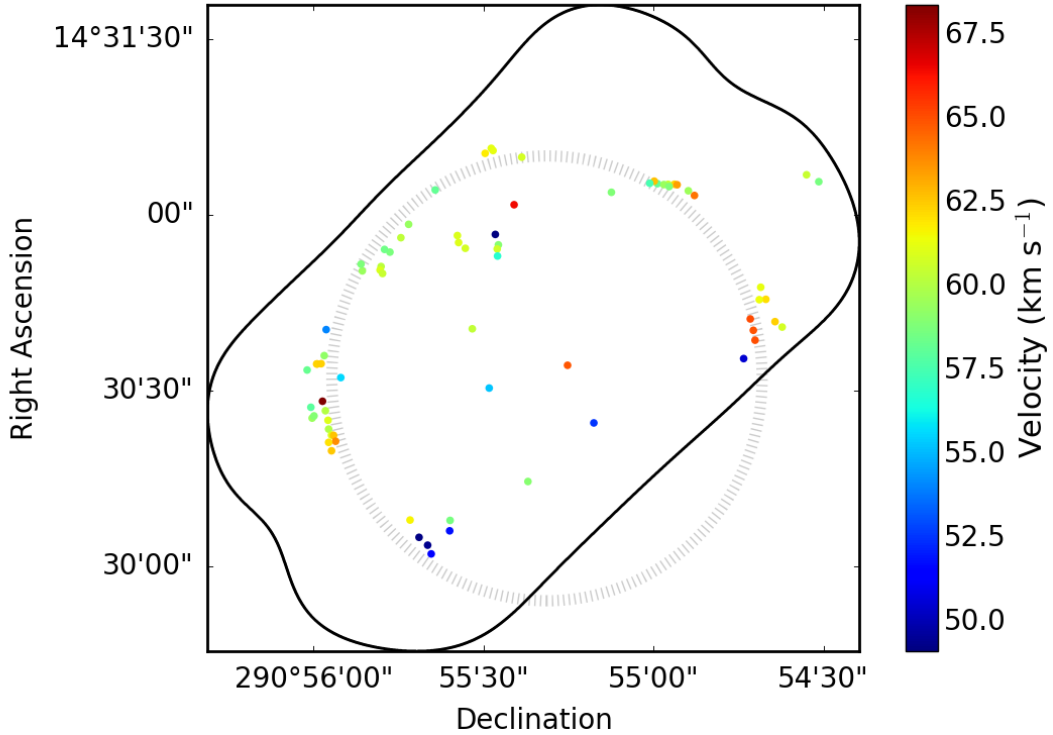


Fig. C.1. The spatial distribution of the hand-identified core sample. The black outer contour shows the observed field of view. The dashed circle shows a hypothetical ring of star formation.

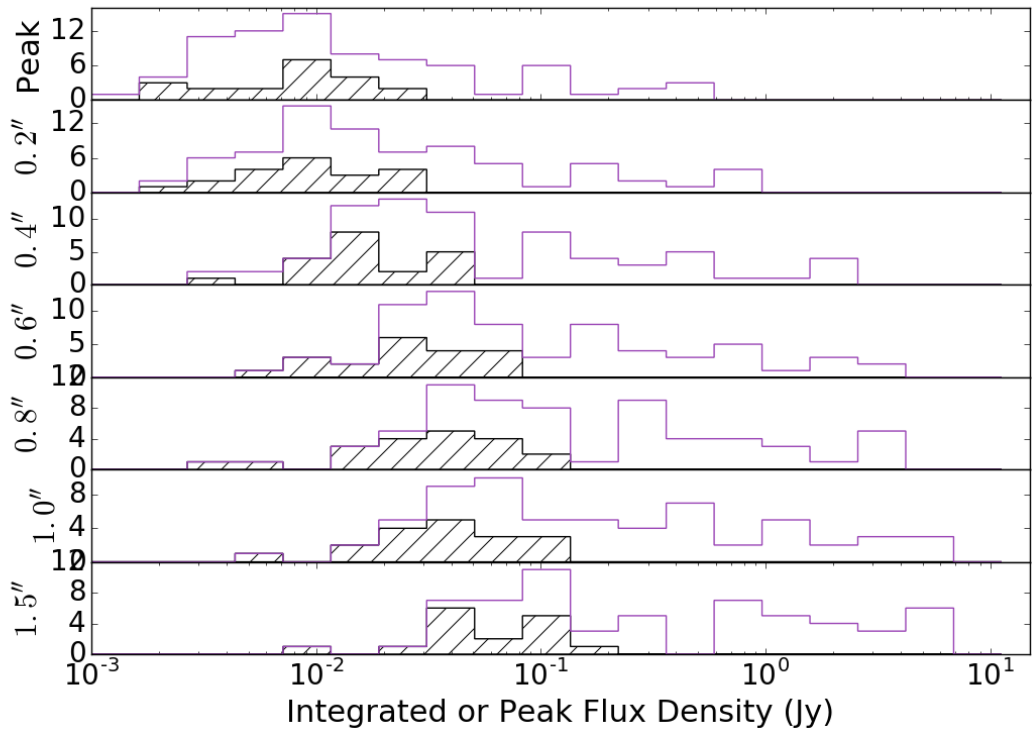


Fig. C.2. Histograms of the core flux densities measured with circular apertures centered on the hand-extracted core positions. The aperture size is listed in the y-axis label. For the top plot, labeled 'Peak', this is the peak flux density in Jy/beam. For the rest, it is the integrated flux density in the specified aperture. The unfilled data show all sources and the hashed data are for starless core candidates (Section C.4). See Figure C.5 for the corresponding masses.

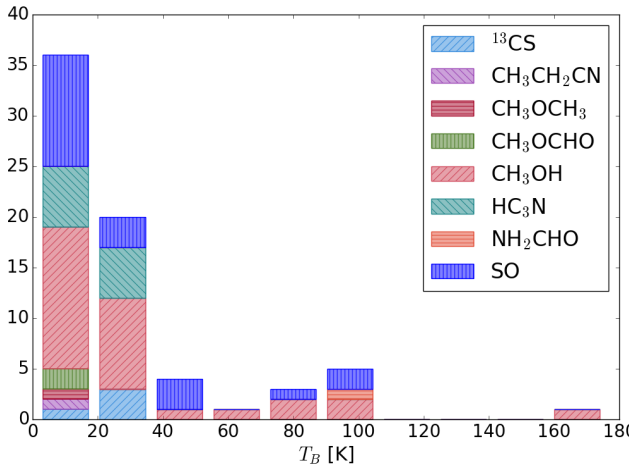


Fig. C.3. Histogram of the brightest line toward each continuum source. The bars are colored by the molecular species associated with the brightest line that is not associated with extended molecular cloud emission, i.e., CO and its isotopologues and H₂CO are excluded.

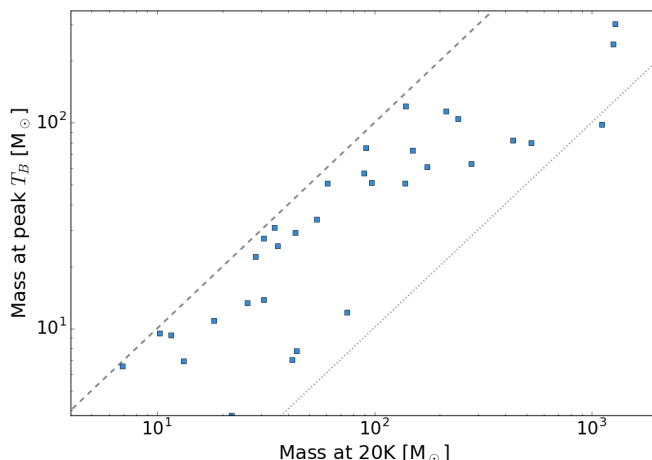


Fig. C.4. The mass computed assuming the dust temperature is the peak brightness temperature vs. that computed assuming $T_{dust} = 20$ K for the aperture extracted continuum sources. The dashed line shows $M(T_{B,max}) = M(20\text{K})$ and the dashed line shows $M(T_{B,max}) = 0.1M(20\text{K})$

In the continuum, we measured a ‘concentration parameter’, which is the ratio of the flux density in a $0.2''$ aperture to that in a $0.2''$ - $0.4''$ annulus divided by three to account for the annulus’ larger area. A uniform source with $r > 0.4''$ source would have a concentration $C = 1$ by this definition, while an unresolved point source would have a Gaussian profile resulting in $C = 14$. Only one source approaches this extreme, the HII region e5, while the rest have $C \leq 7$. We set the threshold for a ‘concentrated’ source to be $C > 2$, which is arbitrary, but does a reasonable job of distinguishing the sources with a clear central concentration from those that have none.

Main sequence OB stars and their illuminated ionized nebulae are in principle easily identified by their free-free emission. Starless cores, protostellar cores, and their variants are more difficult to identify, so we used a combination of temperature and concentration parameter to classify them.

We classified each of the 75 hand-selected sources on the following parameters:

1. Free-free dominated sources ($S_{15\text{GHz}} > 0.5S_{226\text{GHz}}$) are H II regions
2. Free-free contaminated sources ($S_{15\text{GHz}} > 0.1S_{226\text{GHz}}$) are likely to be dust-dominated but with H II region contamination; these are either dusty sources superposed on or embedded in a large H II region or they are compact, dusty H II regions
3. Starless core candidates were identified as those with cold peak brightness temperatures $T_B < 20$ K and with a high concentration parameter ($C > 2$)
4. Hot core candidates are those with peak $T_B > 50$ K and $C > 2$
5. Extended cold core and hot core candidates are those with $T_B < 20$ and $T_B > 50$ K and $C < 2$
6. The remaining sources with $S_{15\text{GHz}} < 0.1S_{226\text{GHz}}$ and $50 > T_B > 20$ K were classed as uncertain compact ($C > 2$) or uncertain extended ($C < 2$)

These classifications are set in the ‘Categories’ column of Table C.2. They serve as a broad guideline for further analysis.

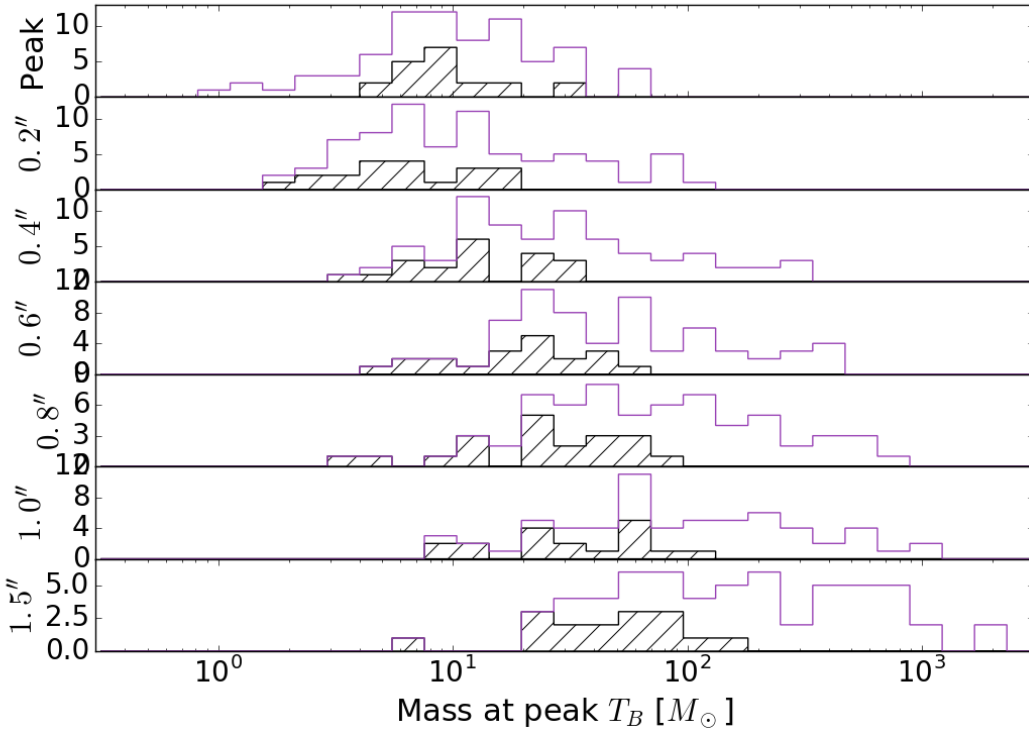


Fig. C.5. Histograms of the core masses computed from the flux density measurements shown in Figure C.2 using the peak brightness temperature toward the center of that source as the dust temperature. The aperture size is listed in the y-axis label. For the top plot, labeled ‘Peak’, the mass is computed from peak flux density in Jy/beam. For the rest, it is the integrated flux density in the specified aperture in Jy. The unfilled data show all sources and the hashed data are for starless core candidates (Section C.4).